Segregation at interfaces in *(GaIn)As/Ga(AsSb)/(GaIn)As*- quantum well heterostructures explored by atomic resolution STEM

P. Kükelhan, S. Firoozabadi, A. Beyer, L. Duschek, C. Fuchs, J. O. Oelerich,

W. Stolz, K. Volz

Materials Science Centre and Faculty of Physics, Philipps University Marburg, Hans-Meerwein-Straße 6, Marburg, Germany

pirmin.kuekelhan@physik.uni-marburg.de Tel +49 64212825713,

Fax +49 642128935

Keywords

A1.Characterization; A3.Metalorganic vapour phase epitaxy; A3.Quantum wells; B2.Semiconducting III-V materials; B3.Solid state lasers

Abstract

Surface segregation and interaction effects of *In* and *Sb* in *(GaIn)As/Ga(AsSb)/(GaIn)As*- "W"-type quantum well heterostructures ("W"-QWHs) are investigated by high angle annular dark field scanning transmission electron microscopy with atomic resolution. "W"-QWHs are promising candidates for type-II laser applications in telecommunications. In this study, independent *(GaIn)As* and Ga(AsSb) quantum wells as well as complete "W"-QWHs are grown by metal organic vapour phase epitaxy on *GaAs* substrate. The composition is determined with atomic

resolution by comparison of the experimental data to complementary contrast simulations. From concentration profiles, an altered segregation in “W”-QWHs in comparison to single *(GaIn)As* and *Ga(AsSb)* quantum wells grown on *GaAs* is detected. *In* and *Sb* are clearly influencing each other during the growth, including blocking effects of *In* incorporation by *Sb* and vice versa. Especially, growth rate and total amount of *Sb* incorporated into *Ga(AsSb)* are decreased by *In* being present.

1. Introduction

Modern semiconductor lasers emitting in the infrared regime are promising for application in telecommunications [1]. So called “W”-type quantum heterostructures (“W”-QWHs) are candidates for laser applications at 1300 nm, which allow more efficient optical telecommunications. In our case, “W”-QWHs are type-II laser systems with an active region consisting of a *Ga(AsSb)* quantum well (QW) embedded between two *(GaIn)As-QWs*. The name “W”-QWH is based on the shape of the resulting band structure. In type-II laser systems, electrons and holes are spatially separated in those different QWs and recombination takes place across the interfaces. Hence, the structure of these interfaces is of major importance for a device’s performance.

The “W”-QWH was theoretically proposed [2–4], successfully grown [5] and was already used for a vertical-external-cavity surface-emitting laser emitting at 1200 nm [6]. To finally achieve efficient laser devices at high emission wavelength, optimization is based on additional characterization of the structures. First optical characterization can be carried out by photoluminescence measurements, while structural characterization is possible by X-ray diffraction (XRD) [5]. To achieve structural characterization with atomic resolution, high angle annular dark field

scanning transmission electron microscopy (HAADF-STEM) is suitable. Due to dominant Z-contrast in HAADF-STEM images, also composition quantification is possible. This can lead to composition determination at an atomic scale [7,8]. Complementary contrast simulations are a common option to achieve this [9]. These simulations can precisely match experimental results [10,11]. Given an atomically resolved composition, effects during growth like surface segregation or interactions between different elements can be investigated at an atomic level.

Surface segregation was shown to play an important role for the growth of *(GaIn)As*- [12] and *Ga(AsSb)*-QWs [13] on *GaAs* and is especially altering their respective interfaces. Several models were proposed to describe the resulting concentration profiles. Among others, these include a phenomenological model by Muraki et al. [14] and a three-layer exchange model proposed by Godbey and Ancona [15]. The Muraki model was successfully applied to *(GaIn)As*- and *Ga(AsSb)*-QWs characterized by TEM methods [16–19] and is widely accepted. The three-layer exchange model was originally tailored for describing surface segregation for *SiGe/Si* but was also used to describe a material system with simultaneous segregation of *In* and *Sb* [20]. Furthermore, interaction mechanisms between *In* and *Sb* during growth were reported before [21].

Beforehand, the “W”-QWH were investigated by HAADF-STEM and intensity profiles obtained were discussed to explore the general structure [22].

In this work, a superior method for local composition determination is applied that is used to isolate the interaction effects in the “W”-QWH by comparison to single QWs. The “W”-QWH as well as single *(GaIn)As*- and *Ga(AsSb)*-QWs are investigated by HAADF-STEM and through comparison with complementary contrast simulations the composition of these QWHs is determined on an atomic level. For the composition

profiles obtained, the Muraki model as well as the three-layer exchange model are applied to all QWHs to quantify segregation. Growth conditions are kept the same for all *(GaIn)As*-QWs and *Ga(AsSb)*-QWs, respectively. Hence, the interaction of *In* and *Sb* in the “W”-QWH can be investigated. In particular, the influence of *Sb* on the surface segregation of *In* and vice versa is analysed.

To this end, first experimental methods used are described in detail. A close discussion of surface segregation and models to characterize it is following. Then, the determined composition of the QWHs and modelling of their present surface segregation are shown. Finally, the accuracy of the composition determination and interaction effects of *In* and *Sb* during the growth are discussed.

2. Materials and Methods

The investigated sample includes a single *(GaIn)As*-QW, a single *Ga(AsSb)*-QW and a “W”-QWH between *GaAs*-barriers. It was grown for the purpose of TEM investigations by MOVPE using an AIXTRON AIX 200 GFR (Gas Foil Rotation) reactor system (Aixtron SE, Herzogenrath, Germany). The growth was carried out on exactly oriented, semi-insulating *GaAs* (001) substrates. As group III precursors triethylgallium (TEGa) and trimethylindium (TMIn) were used, while group V precursors were tertiarybutylarsine (TBAs) and triethylantimony (TESb). The partial pressures of the precursors which were smaller than 1mbar and the high-purity H_2 carrier gas added up to a reactor pressure of 50 mbar. Prior to the sample growth at 550°C [5], the native oxide layer was removed from the substrates by a TBAs-stabilised bake-out procedure. The V/III ratios were chosen as 5.2 for *GaAs*, 3.9 for *(GaIn)As* and 7.4 for *Ga(AsSb)*. In more detail, the ratio of the partial pressure of TMIn to all group III precursors was 0.75, while the ratio of the partial pressure of

TESb to all group V precursors was 0.808. The growth of the *(GaIn)As*- and *Ga(AsSb)*-QWs in the “W”-QWH took place under the exact same conditions as for the single *(GaIn)As*- and *Ga(AsSb)*-QWs. No special gas switching sequence was applied at the interfaces. This allows to investigate the presence of any interaction between In and Sb at the interfaces of the “inner” QW, where both elements are present at the same time.

The sample described above was conventionally prepared for cross-sectional TEM investigations in [010]-direction. Mechanical grinding and polishing was carried out with a Multiprep^{TM} system (Allied High Tech Products, Inc., Rancho Dominguez, CA, United States) down to a thickness of approximately 20 µm, whereas the final thinning and polishing through *Ar*-ion bombardment took place with a precision ion polishing system (model 691 Gatan, Inc., Pleasanton, CA, United States). To limit amorphous layers, the acceleration voltage was gradually decreased from 5 kV to 1.2 kV with an inclination angle of the ion beam on the sample surface of 6°. Due to this preparation procedure, the resulting TEM sample shows a wedge shape, i.e. a thickness gradient. Prior to STEM investigations, the sample was plasma cleaned to remove contaminations (model 1020 E. A. Fischione Instruments, Inc., Export, PA, United States).

HAADF-STEM investigations were performed with a double Cs-corrected JEOL JEM2200FS (JEOL Ltd., Tokyo, Japan) at 200 kV acceleration voltage. The convergence semi-angle of the electron probe of $\alpha = 21.3$ mrad was formed by a condenser aperture with a size of 40 µm. The JEOL EM-24590YPDFI dark-field image detector was detecting electrons scattered to an angular range of 63-252 mrad, 60-240 mrad and 62-248 mrad for the evaluated STEM images of the single *(GaIn)As*-QW, the single *Ga(AsSb)*-QW and the “W”-QWH, respectively. This angular range was determined by measuring the shadow of the detector on a CCD camera to

identify the inner angle [23] while the outer angle is four times the inner angle. Slightly different detector angles are most likely caused by slight changes in the excitation of the filter lenses in different sessions. Each STEM image is the average of ten images with a dwell time of 3 µs per pixel which have been aligned using the software Smart Align [24]. Additionally, the images were normalised to the impinging beam with the help of a beam image [25] on a CCD camera.

To be able to determine the composition of the QWs, complementary image simulations were performed with the software package STEMsalabim [26] which is based on the multi slice method [27]. Chromatic aberration is taken into account by a defocus series [28] of 7 different defoci centred at $\Delta f = 0$ nm with a full width half maximum of 7.5 nm [11]. Thermal diffuse scattering is incorporated by the frozen phonon approximation [29] with 10 different atomic configurations per defocus. Each atomic configuration represents a thermal vibration by statistically displacing atoms from their resting positions. All main parameters for the image simulation corresponding to experimental conditions are found in Table 1. 20 different super cells with a size of 5 x 5 x 80 unit cells (X x Y x Z) were simulated. For ten of them, *(GaIn)As* was simulated for *In* concentrations ranging from 0% to 45%. Likewise, ten super cells of *Ga(AsSb)* with *Sb* concentrations from 0% to 45% were simulated. In all super cells, *In* respectively *Sb* were statistically distributed while fixing the concentration in the whole super cell to the desired value. All super cells were relaxed by valence force field relaxation [30] to consider static atomic displacement.

Electron energy	200 kV
Aperture angle	21.3 mrad
Two-fold astigmatism	0 nm
C_S	2 µm
C_5	5 mm
C_C	1.5 mm

Table 1: Parameters used for simulation of *(GaIn)As* and *Ga(AsSb)* with varying composition. The parameters were determined from the electron microscope used.

3. Segregation models

Surface segregation is well known for III-V heterostructures both grown by molecular beam epitaxy (MBE) [12] and by MOVPE [14]. After its first observation [31,32] and further studies [12] several models to describe it were developed. Moison et al. [33] came up with a thermodynamic model that worked well for high temperatures and small bulk layer concentrations. For lower temperatures, Dehaese et al. [34] proposed a kinetic model that is equivalent to the one by Moison et al. for higher temperatures. However, both models are only working for small bulk concentrations [35,36]. Muraki et al. [14] used a phenomenological model in which for every layer a certain fraction S (segregation coefficient) of incoming atoms is segregating to the surface layer while the rest is incorporated into the crystal. With this, for every layer the concentration x(n) of the segregating element in layer n can be described as

$$x(n) = \begin{cases} x_0(1 - S^n) & : 1 \leq n \leq N \\ x_0(1 - S^n)S^{n-N} & : n > N \end{cases} \quad (1)$$

where x_0 is the final concentration of the segregating element and N is the total number of deposited layers. The segregation model by Muraki et al. was used for several studies of segregation in III-V heterostructures by TEM, especially for *(GaIn)As* [17–19]. In the case of *Sb* segregation, there are also studies available [37]. Additionally, the Muraki model was applied to *InAs/GaSb* super lattices [38]. In all these cases, the Muraki model gives a reasonable description of the experimental findings.

However, it was shown that in certain cases the Muraki model breaks down and the fluid three-layer exchange (F3LE) model proposed by Godbey and Ancona [15] can offer a better description. This was found initially for *SiGe/Si* where extended tails in the concentration profile, i.e. a slow decay of the concentration, were present [39,40]. Additionally, this was reported for a material system where both *In* and *Sb*

segregation are taking place and competing with one another [20]. In contrast to the previous models where only exchange between two layers is considered, in the F3LE model exchange can take place between the three topmost layers and an infinite surface diffusion rate is assumed. When the growth of new layer s starts, the exchange takes place between the topmost layer s and the second topmost layer s-1 and between the second topmost layer s-1 and the third topmost layer s-2. Once layer s is fully grown, layer s-2 is not included in the exchange mechanism anymore and a new layer starts to grow. Hence, growth and exchange take place simultaneously.

For better readability, the following equations describing the F3LE model are given for the case of *In/Ga* but can analogously be used for *Sb/As*. The composition of the three topmost layers taking part in the exchange program is given as

$$X_{In}^{(s)} + X_{Ga}^{(s)} = \frac{t}{\tau} \tag{2}$$

$$X_{In}^{(s-1)} + X_{Ga}^{(s-1)} = 1 \tag{3}$$

$$X_{In}^{(s-2)} + X_{Ga}^{(s-2)} = 1 \tag{4}$$

Here, $X_{In/Ga}^{(s)}$, $X_{In/Ga}^{(s-1)}$, $X_{In/Ga}^{(s-2)}$ denote the concentration of *In* respectively *Ga* in the topmost, second topmost and third topmost layer, t is the time and τ is the time needed to complete the growth of one monolayer. Note, that group III and group V lattices are treated separately. The concentrations of *In* in all three layers underlie mass balance equations:

$$\frac{dX_{In}^{(s)}}{dt} = \Phi_{In} + E_{s,s-1} \tag{5}$$

$$\frac{dX_{In}^{(s-1)}}{dt} = E_{s,s-1} + E_{s-1,s-2} \tag{6}$$

$$\frac{dX_{In}^{(s-2)}}{dt} = E_{s-2,s-1} \tag{7}$$

Here, $\Phi_{In} = \frac{x}{\tau}$ is the *In* incorporation rate and $E_{i,j}$ describe the exchange process.

Thereby, $E_{i,j}$ is given as

$$E_{i,i-1} = P_1 X_{Ga}^{(i)} X_{In}^{(i-1)} - P_2 X_{Ga}^{(i-1)} X_{In}^{(i)} \tag{8}$$

with exchange probabilities P_1 and P_2 that are described as $P_1 = \nu_1 e^{-E_1/kT}$ and $P_2 = \nu_2 e^{-E_2/kT}$. E_1 and E_2 are surface and bulk energy, while ν_1 and ν_2 are vibrational frequencies. They describe a combination of surface and bulk lattice vibration and are normally chosen as $10^{13}\ {}^{1}/_{S}$ [34,41]. T is the temperature and k the Boltzmann constant.

In this work, both the Muraki and the F3LE model are used to describe the composition profiles of the different QWHs.

4. Results

In a first step, composition maps of the QWHs are determined from the experimental HAADF-STEM images. The resulting concentration profiles are used to investigate the surface segregation taking place during the growth of QWHs by MOVPE. Therefore, both Muraki and F3LE model are fitted to the concentration profiles.

4.1 Composition determination

To be able to determine the composition of the QWHs from the HAADF-STEM images, first experimental images and the simulated composition series are carefully matched considering detector sensitivity [42] and source size [11]. Here, the source size parameter fitted is not only representing the source size of the electron source. It also involves the influence of amorphous layers that have been introduced by sample

preparation. These amorphous layers, lead to a general redistribution of intensity from the peaks to the background which can be inherently modelled by the source size parameter. Additional influences of amorphous layers [43] are not taken into account. Consequences following from this will be discussed later.

The composition of each atomic column is determined by a comparison of Voronoi intensities [8] of simulation and experiment. By using Voronoi intensities, the influence of surface relaxation of thin TEM samples [44–46] on the intensity assigned to atomic columns is reduced. For composition determination, the local thickness of each atomic column is taken into account. A detailed description and discussion of the composition determination procedure can be found in [47].

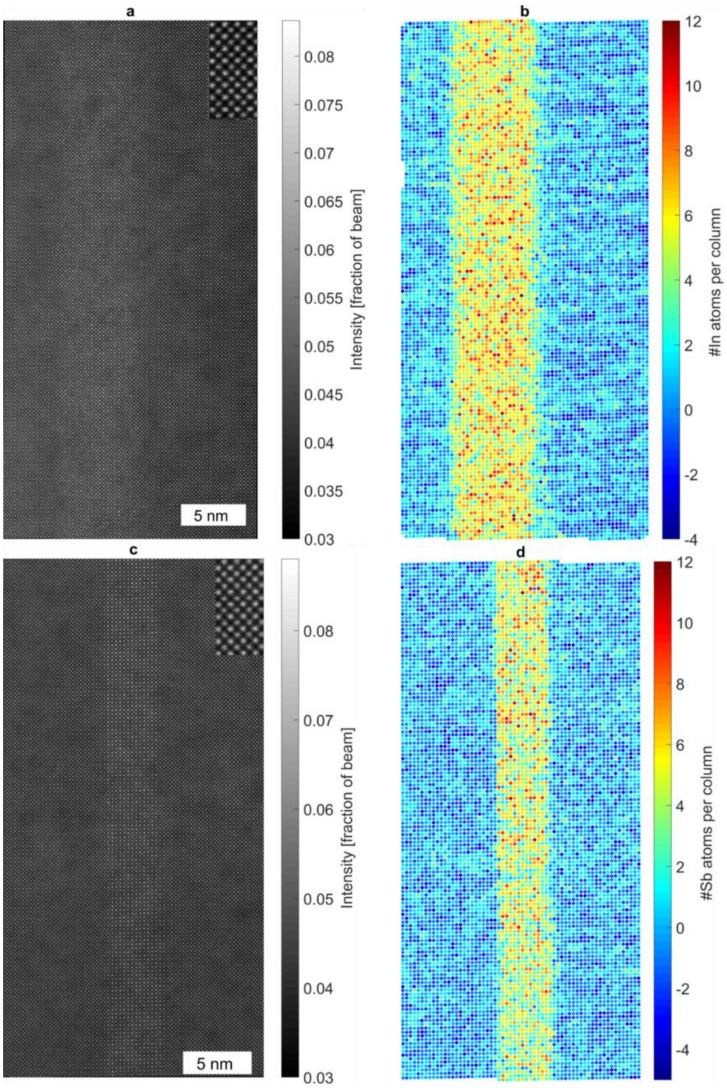

Fig. 1: HAADF-STEM images of the single *(GaIn)As-QW* (A) and the single *Ga(AsSb)*-QW (C). The intensity in both images is normalized to the impinging beam. Magnified insets show the high resolution. Composition maps of the single *(GaIn)As*-QW and the single *Ga(AsSb)*-QW are shown in (B) and (D), respectively. The number of *In* respectively *Sb* is given per atomic column with atomic resolution. Note, that the total number of atoms per column (i.e. the thickness) is not constant within the image. Negative compositions are explained in the main text. Growth direction is from left to right.

The HAADF-STEM images of the single *(GaIn)As*-QW (Fig. 1A) and the single *Ga(AsSb)*-QW (Fig. 1C) together with the composition maps derived are shown in Fig. 1. In the composition maps, for the *(GaIn)As*-QW (Fig. 1B) only group III columns are shown. For the *Ga(AsSb)*-QW (Fig. 1D), only group V columns are shown. The absolute number of *In* atoms or *Sb* atoms per column is given while the thickness of every atomic column differs. In both cases, the mean concentration of *In* or *Sb* is varying around zero in the *GaAs* barriers. The thickness ranges from 25 to 31 atoms per atomic column in the case of *(GaIn)As* and from 24 to 28 atoms per atomic column in the case of *Ga(AsSb)*. The thickness maps are not shown.

For the “W”-QWH, HAADF-STEM image (Fig. 2A) and the composition maps of *In* where only group III columns are shown (Fig. 2B) and *Sb* where only group V columns are shown (Fig. 2C) are presented in Fig. 2.

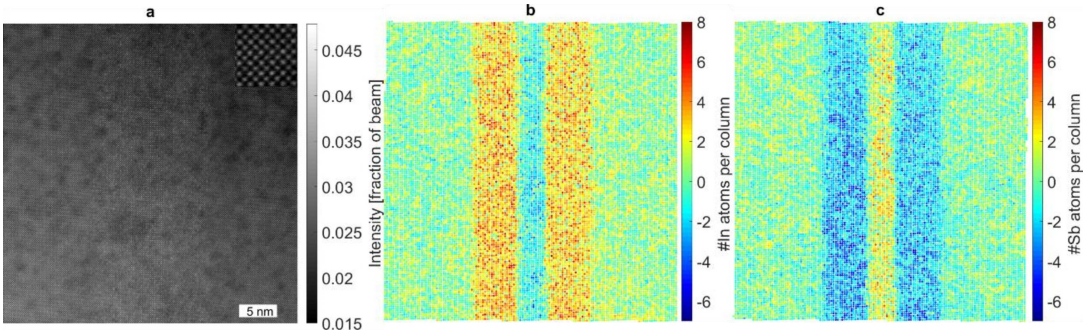

Fig. 2: HAADF-STEM image of the “W”-QWH (A). The intensity is normalized to the impinging beam. A magnified inset shows the high resolution. The composition of *In* is shown in B, while the composition of *Sb* is presented in C. Again, note the varying thickness of the atomic columns. Negative compositions are explained in the text. Growth direction is from left to right.

Here, the thickness of the atomic columns ranges from 10 to 19 atoms per atomic column as the total field of view of the HAADF-STEM image is roughly twice as large as in case of the single QWs. The thickness of every atomic column is determined by using the other sub lattice given a negligible influence of cross scattering [47].
An apparently negative composition of *In* in the *Ga(AsSb)*-QW and an apparently negative composition of *Sb* in the *(GaIn)As*-QWs is determined. This is caused by the local thickness determination that uses the other sub lattice. Consequently, the increased intensity of the other sub lattice due to compositional changes leads to a wrong thickness determination of the group III sub lattice in the *Ga(AsSb)*-QW and the group V sub lattice in the *(GaIn)As*-QWs. Hence, the composition is determined for a wrong thickness which is assumed to be higher than the actual thickness. This leads to unphysical negative compositions. However, since all QWs in the "W"-QWH are ternary the same composition determination procedure can still be used and the negative concentrations in the other QW can be omitted. So, the *In* composition is trustable everywhere but in the *GaAsSb*-QW, while the *Sb* composition is only wrong in the *GaInAs*-QWs. In *GaAs* barriers, the mean concentration of *In* or *Sb* determined is almost zero as expected.

4.2 Surface segregation

From the composition maps, concentration profiles of the QWHs can be obtained by averaging the composition of each lattice plane considering the local thickness of each atomic column. This yields a layer-by-layer concentration profile of the QWHs. For the single *(GaIn)As*-QWs and the *(GaIn)As*-QWs in the "W"-QWH, the concentration profiles are shown in Fig. 3. The "error bars" do not give the accuracy of concentration determination but instead they give the standard deviation of the concentration per lattice plane. As discussed in previous work [22], this standard deviation reflects a Poisson-like distribution of In in the QWs considering the

experimental noise present in the measurement. The experimental noise can be determined in the *GaAs* barrier and could be subtracted to reveal the actual chemical fluctuation of the ternary materials assuming quadratic addition of standard deviations. However, this was not done in the given profiles.

The concentration profile of the single *(GaIn)As*-QW clearly shows surface segregation well known for III-V heterostructures [16]. In a first step, the Muraki model is fitted to all *(GaIn)As*-QW of the *(GaIn)As*-QWs in the "W"- using the Levenberg-Marquardt algorithm [48]. The concentration profiles together with the fitted models are shown in Fig. 3. As inset, the fitting parameters of the Muraki model are given together with the R^2-value of the fit. For better visualization, for every concentration the data point (0/0) was added. However, this does not change the fit of the Muraki model.

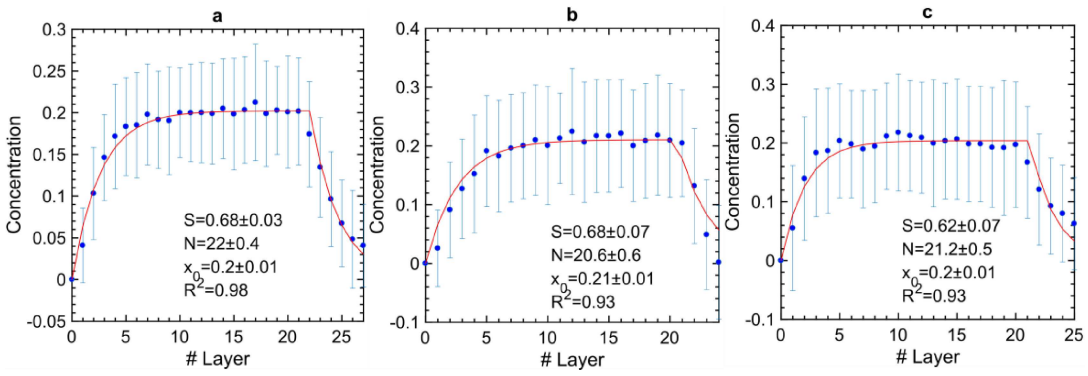

Fig. 3: Muraki model fitted to the composition profiles of the single *(GaIn)As*-QW (A), the first *(GaIn)As*-QW in the "W"-QWH (B) and the second *(GaIn)As*-QW in the "W"-QWH. The concentration of *In* is given as fraction averaged over one atomic layer considering the local thickness of each atomic column. Shown error bars do not indicate the error of composition determination but the standard deviation per lattice plane. Fit parameters are given as insets.

To specify the different interfaces, for each QW the first interface in growth direction is called lower interface, while the second interface in growth direction is called the upper interface. This nomenclature is chosen based on the geometry during growth. For the single *(GaIn)As*-QW (Fig. 3A), a very good description of the concentration profile is achieved with the Muraki model. This is true for both the lower and the upper interface. The segregation coefficient determined as $S = 0.68 \pm 0.03$ is in good agreement with the value of $S = 0.65 \pm 0.05$ found by Piscopiello et al. [17] for *(GaIn)As* also grown by MOVPE at 550°C.

Furthermore, the Muraki model is fitted to all the *(GaIn)As*-QWs in the "W"-QWH. For the first *(GaIn)As*-QW in the "W"-QWH (in growth direction, Fig. 3B), the same segregation coefficient as for the single *(GaIn)As*-QW was found ($S = 0.68 \pm 0.07$). However, the fit is not describing the data as well as in the previous case. Especially at the upper interface where the concentration decreases and the Ga(AsSb)-QW is already grown, the concentration profile is not well matched.

For the second *(GaIn)As*-QW in the "W"-QWH (Fig. 3C), the segregation coefficient determined is slightly lower $S = 0.62 \pm 0.07$ but within the errors the segregation coefficients of both *(GaIn)As*-QWs agree. Again, the data is not well matched by the Muraki model everywhere: Lower (growth on *Ga(AsSb)*) as well as upper interface (followed by *GaAs*) of the concentration show some deviations from the Muraki model.

The Muraki model is also applied to the *Ga(AsSb)*-QWs. For the single *Ga(AsSb)*-QW (Fig. 4A), the Muraki model is reasonably describing the concentration profile of *Sb* in the QW. In case of the *Ga(AsSb)*-QW in the "W"-QWH (Fig. 4B), the Muraki model is also matching the *Sb* concentration profile reasonably.

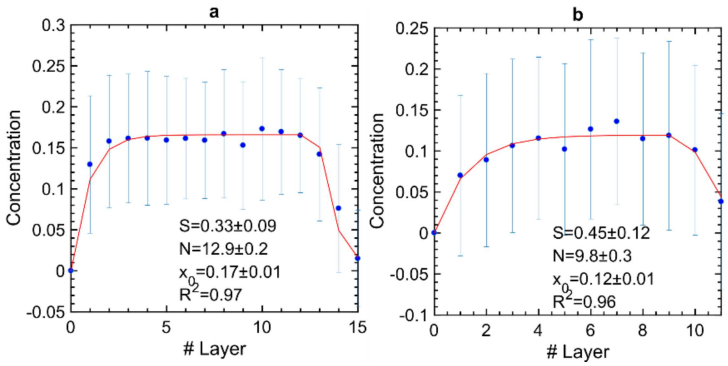

Fig. 4: Muraki model fitted to the composition profiles of the single *Ga(AsSb)*-QW (A) and the *Ga(AsSb)*-QW in the "W"-QWH (B). The concentration of *Sb* is given as fraction averaged over one atomic layer considering the local thickness of each atomic column. Shown error bars do not indicate the error of composition determination but the standard deviation per lattice plane. Fit parameters are given as insets.

Since the Muraki model is not matching all concentration profiles additionally the F3LE model by Godbey and Ancona is considered to describe the concentration profiles. This model is chosen because in previous studies it has been shown that the F3LE model can describe concentration profiles in certain cases where the Muraki model fails.

For this, the resulting partial differential equations have to be solved and fitted to the concentration profiles. Fitting is performed with the Nelder-Mead method [49].

The time to grow one monolayer τ is determined from the growth time for the QWs which is 11s in case of the *(GaIn)As*-QWs and 13s in case of the *Ga(AsSb)*-QWs and the number of layers as determined by the Muraki model.

The results for the *(GaIn)As*-QWs are shown in Fig. 5. For the single *(GaIn)As*-QW (a), a very good description can be achieved. In case of the first *(GaIn)As*-QW in the "W"-QWH, the data is also described well by the model with slightly changed energies. For the second *(GaIn)As*-QW in the "W"-QWH, the description is less accurate at the interfaces.

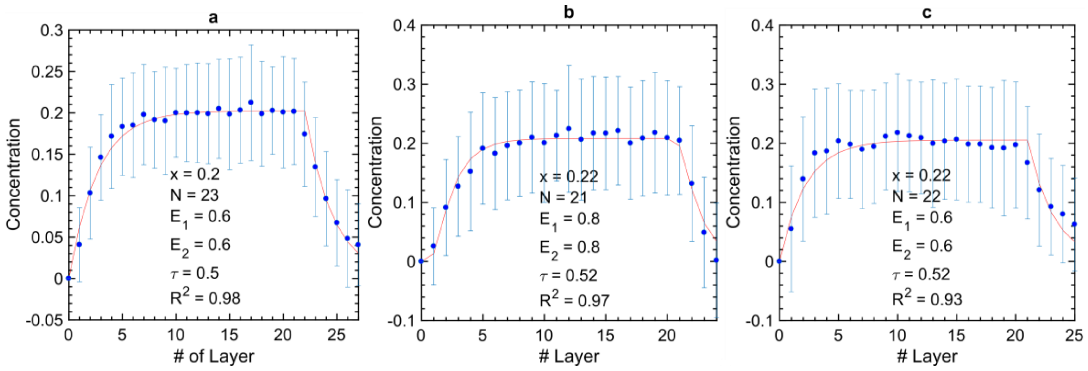

Fig. 5: F3LE model fitted to *(GaIn)As*-QWs. The results for the single QW (A) and the first (B) and second (C) QW in the "W"-QWH are shown together with the parameters used. Energies are given in eV. The parameter N describes the layer after which In deposition stops.

For the single *Ga(AsSb)*-QW, also a very good description of the concentration profile by the F3LE model is possible (Fig. 6(a)). In case of the *Ga(AsSb)*-QW in the "W"-QWH, the agreement of model and data is reasonable considering the small amount of data especially at the interfaces.

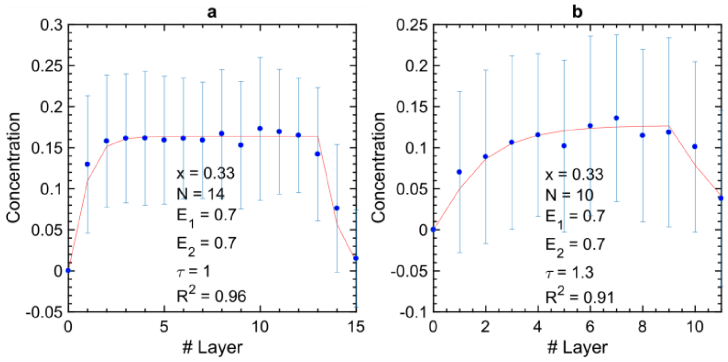

Fig. 6: F3LE model fitted to single *Ga(AsSb)*-QW (A) and *Ga(AsSb)*-QW in the "W"-QWH (B). The fitting parameters are given as insets. Energies are given in eV. The parameter N describes the layer after which Sb deposition stops.

5. Discussion

Below, the results for both composition determination and surface segregation are discussed.

5.1 Accuracy of composition determination

The composition determination of the different QWHs is performed on an atomic scale. Composition determination by comparing experimental and simulated STEM intensities is a statistical process. Different z-height distributions of the substitute atoms can yield the same Voronoi intensity which leads to an inherent uncertainty. For a given atomic column, its composition can be determined with single-atom accuracy with a certain probability depending on material system and thickness. However, if the number of analysed atomic columns is large enough, the overall composition is determined correctly [47].

For composition determination, the local thickness of each atomic column is considered. Additionally, the simulation includes static atomic displacements and accurate modelling of the electron microscope. However, there are still several parameters which were not thoroughly considered in the evaluation process: surface relaxation, amorphous layers on the samples and inelastic scattering.

The surface relaxation of thin TEM samples can have a severe influence on the intensities used for quantitative STEM evaluations [45,46]. This influence is reduced by the use of Voronoi cells as already stated above. Additionally, the influence of surface relaxation is picked up by local thickness treatment that factors in the local intensity of each column. If surface relaxation changes Voronoi intensities locally, this leads to a thickness determination deviating from the real one. Finally, this also has an influence on the concentration determination. However, for the QWs investigated surface relaxation plays a minor role, since the strain is comparably low.

Furthermore, a thorough consideration of surface segregation is not trivial since the actual sample structure and geometry, e.g. QW width, composition and sample thickness, affects the way surface relaxation alters the intensity [45].

Amorphous layers occur both on top and bottom of the crystalline centre as ion bombardment during sample preparation is destroying the crystalline sample. For *GaAs* based materials prepared in the same way as in this work, the thickness of the amorphous layers both on top and bottom was found to be 3.5 nm [50]. Hence, the thickness of the amorphous layers present on the investigated sample is expected to be in a similar range. Both amorphous layers lead to an increase of the detected scattered intensity whereby the influence is larger for smaller detector angles. The true crystalline thickness will be smaller than the one determined without considering amorphous layers. However, if different amorphous materials behave very similar for their intensity increase as proposed for the case of *Si* and *Ge* by Grieb et al. [51], then the concentration finally derived should not change. Besides the general intensity increase, the amorphous layer on the top surface also broadens the beam and leads to enhanced cross scattering compared to a fully crystalline sample. Taking into account amorphous layers for quantitative STEM in general and for thickness determination in particular can be achieved by considering them in simulations or removing them on the experimental sample by very low voltage ion bombardment [52]. Simulation involving methods can be based on position averaged convergent electron beam diffraction for the determination of crystalline thickness, e.g. like suggested by Grieb et al. [51].

Inelastic scattering is not considered for the simulation when comparing experimental and simulated intensities. However, inelastic scattering is less important for high angles used here [53] so the measurements in this work performed for an angular range above 60 mrad are not affected.

In the composition maps, non-zero concentrations of *In* respectively *Sb* in *GaAs* regions are present. On the one hand, these can be caused by the determination of the local thickness as discussed in detail elsewhere [47]. On the other hand, the non-

zero concentrations are a consequence of the material system investigated. The local thickness of each column is determined through *Ga* or *As* columns with a precision of one atom by comparison of its Voronoi intensity to simulations. The atomic number of the column is the main factor for the scattered intensity of that atomic column. If the thickness of a column is increased by one *Ga* or *As* column, the total atomic number *Z* of that column is increased by 31 or 33, respectively. In comparison, replacing a *Ga* atom by an *In* atom or *As* by *Sb* increases the total atomic number of that column by only 18. Hence, one additional *Ga* or *As* atom (i.e. changing the thickness) has a larger impact on the intensity of that column than changing the composition: The "composition sampling" of the intensity is smaller than the "thickness sampling" of the intensity. Since all thicknesses and compositions are found by matching intensities of simulation and experiment, this leads to non-zero compositions of columns in *GaAs*. Of course, the same effect is also happening in QWs. An ideal material system for composition determination consists of materials where the influence of a thickness change is smaller than that of a composition change. The small deviation from zero of the mean concentrations in *GaAs* is most likely caused by the presence of the amorphous layer. For further discussion of the composition determination, also see [47].

In general, the composition determination method used is giving an excellent agreement of the composition of the *(GaIn)As*-QW with the composition determined by XRD and a reasonable agreement for the *Ga(AsSb)*-QW. The deviations in case of *Ga(AsSb)* could be explained by a stronger oxidation of the surfaces of the TEM specimen in the Sb containing layer [54].

5.2 Interaction of *In* and *Sb* during growth

Since the growth conditions of the single QWs and the QWs in the “W”-QWH are exactly the same, a comparison of the resulting concentration profiles of the QWs gives insight into the influences of *In* and *Sb* on each other during the growth.

First, the single *(GaIn)As*-QW and the two *(GaIn)As*-QWs in the “W”-QWH are compared to each other.

All *(GaIn)As*-QWs have the same maximum *In* concentration of $x \approx 0.2$ but the shape, i.e. the surface segregation, differs depending on the material at the interface that is either *GaAs* or *Ga(AsSb)*.

In case of the single *(GaIn)As*-QW, the Muraki model gives an adequate description of the concentration profile obtained and the surface segregation present as was already reported in several cases before [16–18]. Additionally, the segregation coefficient obtained is in good agreement with results published before for a *(GaIn)As*-QW grown by MOVPE at the same growth temperature. This supports the validity of both concentration profile and segregation coefficient determined. In contrast, the F3LE model does not give a satisfying fit to the concentration of the QW so it can be stated that only the two topmost layers are included in the exchange process taking place during *(GaIn)As* growth.

In the following, descriptions of the segregation for the *(GaIn)As*-QWs in the “W”-QWH are referring to the segregation for the single *(GaIn)As*-QW where all interfaces consist of *GaAs*. To allow for quantitative comparison, the Muraki model is slightly modified. For the lower interface, a segregation coefficient S_l is used while the upper interface is described by segregation coefficient S_u. This is motivated by the inequivalence of lower and upper interface. The resulting model is

$$x(n) = \begin{cases} x_0(1 - S_l^n) & : 1 \leq n \leq N \\ x_0(1 - S_l^n)S_u^{n-N} & : n > N \end{cases} \quad (9)$$

so that both interfaces can be treated independently. In Fig. 7, the fits obtained for the *(GaIn)As*-QWs in the “W”-QWH are shown. Both give a good description of the concentration profiles at both interfaces. The resulting segregation coefficients at both interfaces differ from each other which is discussed hereafter.

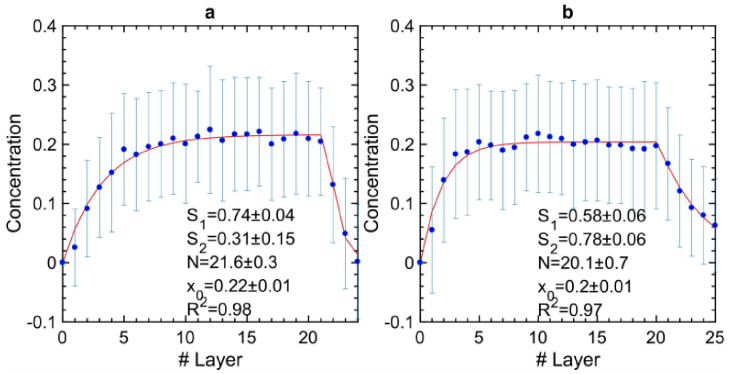

Fig. 7: Modified Muraki model with two different segregation coefficients fitted to the concentration profiles of the first (A) and the second (B) *(GaIn)As*-QW in the “W”-QWH. In both cases, a reasonable description of both interfaces is reached. Fit parameters are given as insets.

The first *(GaIn)As*-QW in the “W”-QWH shows a very similar segregation at the lower interface. This is supported by the segregation coefficients determined with the Muraki model ($S_l^I = 0.74 \pm 0.04$). Since both QWs are grown on *GaAs* under the same growth conditions this is the expected result. A decrease in concentration takes place when the *In* supply during growth is stopped. Depending on the present segregation, this concentration decrease can take place slowly as it is the case for the single *(GaIn)As*-QW. In contrast, the first *(GaIn)As*-QW in the “W”-QWH shows an abrupt decay of *In* concentration. Consequently, a smaller segregation coefficient for the upper interface of $S_u^I = 0.31 \pm 0.15$) is connected to this abrupt decay. Since only a limited amount of data points is used for fitting, a larger error results. The abrupt decay is in agreement with results published by Sanchez et al. [21] who found blocking of incorporation of segregating *In* by *Sb*. The growth of *Ga(AsSb)* on the first *(GaIn)As*-QW can stop *In* incorporation. So, the blocking of segregating *In* leads to

an abrupt interface. While the segregation at the lower interface of the first *(GaIn)As*-QW in the “W”-QWH is the same as for the single *(GaIn)As*-QW, the upper interface is altered and surface segregation is suppressed due to the interface to the *Ga(AsSb)*-QW in the “W”-QWH.

In line with blocking of *In* incorporation by *Sb*, the lower interface of the second *(GaIn)As*-QW in the “W”-QWH deviates from the one of the other *(GaIn)As*-QWs that is dominated by segregation. It does not show the same degree of surface segregation and is more abrupt ($S_l^{II} = 0.58 \pm 0.06$). This can be explained by the fact that this *(GaIn)As*-QW is grown on *Ga(AsSb)* instead on *GaAs*.

Furthermore, this is connected to blocking of *In* incorporation. The amount of *Sb* still present from the growth of the *Ga(AsSb)*-QW has to drop below a certain value before the growth of the second *(GaIn)As*-QW can start. Once this value is undercut, the incorporation of *In* already offered and presumably floating on the surface can begin which leads to a more abrupt interface and less surface segregation developing.

The concentration decrease at the upper interface is taking place with a higher segregation coefficient again ($S_u^{II} = 0.76 \pm 0.06$). This surface segregation is similar to the single *(GaIn)As*-QW as both QWs are followed by *GaAs*. However, the segregation coefficient is slightly increased. This can be connected to the growth on already strained layers in the “W”-QWH. Summarized, the surface segregation of the second *(GaIn)As*-QW in the “W”-QWH at the lower interface is changed due to the *Ga(AsSb)*-QW it is grown on and the *Sb* blocking *In* incorporation until the *Sb* content has undercut a certain value whereas the upper interface remains almost unchanged.

All in all, the *(GaIn)As*-QWs in the “W”-QWH are severely altered with regard to their surface segregation where they have interfaces to the *Ga(AsSb)*-QW but show the same surface segregation as in case of the single *(GaIn)As*-QW otherwise.

A comparison of the single *Ga(AsSb)*-QW and the one inside the “W”-QWH shows huge differences. The concentration of *Sb* in the *Ga(AsSb)*-QW inside the “W”-QWH is significantly decreased. Apparently, the growth of *Ga(AsSb)* on *(GaIn)As* (in combination with *In* possibly still floating on the surface) decreases the incorporation of *Sb* even more severely as the other way around. This is in agreement with findings reported by Sanchez et al. [21]. They found an *GaSb* layer on *(GaIn)As* that was intended to contain 100 % of *Sb* to have an *Sb* concentration of only 5%. A possible explanation would be disruption of the surface coverage of *Sb* by the floating *In* layer since a critical amount is needed [13].

Additionally, the QW inside the “W”-QWH has a noticeably smaller width than the single one (10 vs. 13 atomic layers). Here, the combination of a *(GaIn)As*-QW before the *Ga(AsSb)*-QW, *In* possibly still floating on the surface and a *(GaIn)As*-QW grown afterwards (i.e. newly incoming *In* floating on the surface) is limiting the incorporation of *Sb*, i.e. the growth rate of *Ga(AsSb)* is changed by the floating layer of *In*. This could also be connected to the critical surface coverage of *Sb* needed.

The Muraki model gives a reasonable description of the concentration profile of the single *Ga(AsSb)*-QW and the *Ga(AsSb)*-QW in the “W”-QWH. *Sb* surface segregation was described by the Muraki model before [37] so that the single *Ga(AsSb)*-QW is expected to be describable by the Muraki model. The *Ga(AsSb)*-QW in the “W”-QWH has two interfaces to *(GaIn)As*-QWs (lower and upper interface) which is in contrast to the *(GaIn)As*-QWs in the “W”-QWH that have interfaces to two different materials. Hence, the *Ga(AsSb)*-QW in the “W”-QWH can be described by

the Muraki model with one segregation coefficient while the *(GaIn)As*-QWs in the "W"-QWH cannot as has been shown above.

Schowalter et al. [16] empirically related the segregation efficiency to the lattice mismatch between the materials grown. A smaller lattice mismatch leads to a smaller segregation coefficient, i.e. a more abrupt interface.

This relationship was tailored for single QWs and can therefore not easily be applied to QWHs where strain builds up and additional interaction between elements is present as outlined above.

Haxha et al. [20] showed that the F3LE model can be used to describe both *In* and *Sb* segregation of *Ga(AsSb)/InAs* grown by MBE. Here, next to the single QWs we apply it to the "W"-QWH grown by MOVPE. The F3LE model can be used to describe the growth of the first *(GaIn)As*-QW in the "W"-QWH and also the second *(GaIn)As*-QW in the "W"-QWH in presence of *Sb* with reasonable agreement. Additionally, the *Ga(AsSb)*-QW in the "W"-QWH is reasonably described. Hence, the description of the growth is possible when incorporating three layers. The energies describing the exchange between layers are slightly changed compared to the single QWs used as a reference pointing to different growth behaviour in presence of In/*Sb*.

The results from the F3LE model support the statements made about the growth before.

6. Summary

Concentration profiles of single *(GaIn)As*- and *Ga(AsSb)*-QWs as well as of the whole "W"-QWH were determined on an atomic level by STEM and complementary contrast simulations. With these concentration profiles, growth in general and surface segregation in particular was investigated with regard to influences of *In* and *Sb* on each other. Several findings were made: (i) Surface segregation plays a decisive role

in growth of “W”-QWH. (ii) *In* and *Sb* alter surface segregation of each other so that a holistic description by existing models is not possible. (iii) Different segregation coefficients are needed to describe the interfaces of the *(GaIn)As*-QWs in the “W”-QWH as they differ for interfaces to *GaAs* and to *Ga(AsSb)*. (iv) On the one hand, *Sb* is blocking *In* incorporation both after and before the growth of *(GaIn)As*. (v) On the other hand, *In* is changing the growth of *Ga(AsSb)* altering both the total amount of incorporated *Sb* and the growth rate.

In conclusion, surface segregation and interactions between *In* and *Sb* during the growth of “W”-QWHs were revealed using atomic resolution STEM.

Acknowledgements

Financial support by the German Research Foundation (DFG) in the framework of SFB 1083 and GRK 1782 is gratefully acknowledged. S. Firoozabadi acknowledges support of the European Union’s Horizon 2020 in the framework of the project microSPIRE (ID: 766955).

Bibliography

[1] E. Murphy, Enabling optical communication, Nat. Photonics. 4 (2010) 287–287. doi:10.1038/nphoton.2010.107.

[2] J.R. Meyer, C.A. Hoffman, F.J. Bartoli, L.R. Ram-Mohan, Type-II quantum-well lasers for the mid-wavelength infrared, Appl. Phys. Lett. 67 (1995) 757–759. doi:10.1063/1.115216.

[3] M. Kudo, K. Ouchi, J. Kasai, T. Mishima, Low-Lattice-Strain Long-Wavelength GaAsSb/GaInAs Type-II Quantum Wells Grown on GaAs Substrates, Jpn. J. Appl. Phys. 41 (2002) L1040–L1042. doi:10.1143/JJAP.41.L1040.

[4] C. Berger, C. Möller, P. Hens, C. Fuchs, W. Stolz, S.W. Koch, A. Ruiz Perez, J. Hader, J. V. Moloney, Novel type-II material system for laser applications in the near-infrared regime, AIP Adv. 5 (2015) 047105. doi:10.1063/1.4917180.

[5] C. Fuchs, A. Beyer, K. Volz, W. Stolz, MOVPE growth of

(GaIn)As/Ga(AsSb)/(GaIn)As type-II heterostructures on GaAs substrate for near infrared laser applications, J. Cryst. Growth. 464 (2017) 201–205. doi:10.1016/j.jcrysgro.2016.10.052.

[6] C. Möller, C. Fuchs, C. Berger, A. Ruiz Perez, M. Koch, J. Hader, J. V. Moloney, S.W. Koch, W. Stolz, Type-II vertical-external-cavity surface-emitting laser with Watt level output powers at 1.2 μm, Appl. Phys. Lett. 108 (2016). doi:10.1063/1.4942103.

[7] S. Van Aert, J. Verbeeck, R. Erni, S. Bals, M. Luysberg, D. Van Dyck, G. Van Tendeloo, Quantitative atomic resolution mapping using high-angle annular dark field scanning transmission electron microscopy, Ultramicroscopy. 109 (2009) 1236–1244. doi:10.1016/j.ultramic.2009.05.010.

[8] A. Rosenauer, T. Mehrtens, K. Müller, K. Gries, M. Schowalter, P. Venkata Satyam, S. Bley, C. Tessarek, D. Hommel, K. Sebald, M. Seyfried, J. Gutowski, A. Avramescu, K. Engl, S. Lutgen, Composition mapping in InGaN by scanning transmission electron microscopy, Ultramicroscopy. 111 (2011) 1316–1327. doi:10.1016/j.ultramic.2011.04.009.

[9] J.M. LeBeau, S.D. Findlay, L.J. Allen, S. Stemmer, Quantitative atomic resolution scanning transmission electron microscopy, Phys. Rev. Lett. 100 (2008) 206101. doi:10.1103/PhysRevLett.100.206101.

[10] J.M. LeBeau, S.D. Findlay, X. Wang, A.J. Jacobson, L.J. Allen, S. Stemmer, High-angle scattering of fast electrons from crystals containing heavy elements: Simulation and experiment, Phys. Rev. B. 79 (2009) 214110. doi:10.1103/PhysRevB.79.214110.

[11] A. Beyer, J. Belz, N. Knaub, K. Jandieri, K. Volz, Influence of spatial and temporal coherences on atomic resolution high angle annular dark field imaging, Ultramicroscopy. 169 (2016) 1–10. doi:10.1016/j.ultramic.2016.06.006.

[12] J. Massies, F. Turco, A. Saletes, J.P. Contour, Experimental evidence of difference in surface and bulk compositions of AlGaAs, AlInAs and GaInAs epitaxial layers grown by molecular beam epitaxy, J. Cryst. Growth. 80 (1987) 307–314. doi:10.1016/0022-0248(87)90076-5.

[13] M. Pristovsek, M. Zorn, U. Zeimer, M. Weyers, Growth of strained GaAsSb layers on GaAs (001) by MOVPE, J. Cryst. Growth. 276 (2005) 347–353. doi:10.1016/j.jcrysgro.2004.11.420.

[14] K. Muraki, S. Fukatsu, Y. Shiraki, Surface segregation of In atoms during molecular beam epitaxy and its influence on the energy levels in InGaAs/GaAs quantum wells, Appl. Phys. Lett. 61 (1992) 557–559. doi:10.1063/1.107835.

[15] D.J. Godbey, M.G. Ancona, Modeling of Ge segregation in the limits of zero and infinite surface diffusion, J. Vac. Sci. Technol. A Vacuum, Surfaces, Film. 15 (1997) 976–980. doi:10.1116/1.580790.

[16] M. Schowalter, A. Rosenauer, D. Litvinov, D. Gerthsen, Investigation of segregation

by quantitative transmission electron microscopy, Opt. Appl. 36 (2006) 297–308.

[17] E. Piscopiello, A. Rosenauer, A. Passaseo, E.H. Montoya Rossi, G. Van Tendeloo, Segregation in InGaAs/GaAs Stranski–Krastanow layers grown by metal–organic chemical vapour deposition, Philos. Mag. 85 (2005) 3857–3870. doi:10.1080/147830500269402.

[18] D. Litvinov, D. Gerthsen, A. Rosenauer, M. Schowalter, T. Passow, M. Hetterich, The Role of Segregation in InGaAs Heteroepitaxy, Mater. Sci. Forum. 539–543 (2007) 3540–3545. doi:10.4028/www.scientific.net/MSF.539-543.3540.

[19] T. Mehrtens, K. Müller, M. Schowalter, D. Hu, D.M. Schaadt, A. Rosenauer, Measurement of indium concentration profiles and segregation efficiencies from high-angle annular dark field-scanning transmission electron microscopy images, Ultramicroscopy. 131 (2013) 1–9. doi:10.1016/j.ultramic.2013.03.018.

[20] V. Haxha, I. Drouzas, J.M. Ulloa, M. Bozkurt, P.M. Koenraad, D.J. Mowbray, H.Y. Liu, M.J. Steer, M. Hopkinson, M.A. Migliorato, Role of segregation in InAs/GaAs quantum dot structures capped with a GaAsSb strain-reduction layer, Phys. Rev. B. 80 (2009) 165334. doi:10.1103/PhysRevB.80.165334.

[21] A.M. Sanchez, A.M. Beltran, R. Beanland, T. Ben, M.H. Gass, F. De La Pẽa, M. Walls, A.G. Taboada, J.M. Ripalda, S.I. Molina, Blocking of indium incorporation by antimony in III-V-Sb nanostructures, Nanotechnology. 21 (2010) 145606. doi:10.1088/0957-4484/21/14/145606.

[22] P. Kükelhan, A. Beyer, C. Fuchs, M.J. Weseloh, S.W. Koch, W. Stolz, K. Volz, Atomic structure of ‘W’-type quantum well heterostructures investigated by aberration-corrected STEM, J. Microsc. 268 (2017) 259–268. doi:10.1111/jmi.12647.

[23] J.M. LeBeau, S. Stemmer, Experimental quantification of annular dark-field images in scanning transmission electron microscopy, Ultramicroscopy. 108 (2008) 1653–1658. doi:10.1016/j.ultramic.2008.07.001.

[24] L. Jones, H. Yang, T.J. Pennycook, M.S.J. Marshall, S. Van Aert, N.D. Browning, M.R. Castell, P.D. Nellist, S.I. Molina, D.L. Sales, P.L. Galindo, D. Fuster, Y. González, B. Alén, L. González, M. Varela, S.J. Pennycook, R. Erni, H. Heinrich, G. Kostorz, V. Grillo, E. Carlino, F. Glas, F. Rossi, E.J. Kirkland, Z. Yu, P.E. Batson, J. Silcox, E. Carlino, V. Grillo, Smart Align-a new tool for robust non-rigid registration of scanning microscope data, Ultramicroscopy. 109 (2009) 8. doi:10.1186/s40679-015-0008-4.

[25] D.S. He, Z.Y. Li, A practical approach to quantify the ADF detector in STEM, J. Phys. Conf. Ser. 522 (2014) 012017. doi:10.1088/1742-6596/522/1/012017.

[26] J.O. Oelerich, L. Duschek, J. Belz, A. Beyer, S.D. Baranovskii, K. Volz, STEMsalabim: A high-performance computing cluster friendly code for scanning transmission electron microscopy image simulations of thin specimen,

Ultramicroscopy. 177 (2017) 91–96. doi:10.1016/j.ultramic.2017.03.010.

[27] E.J. Kirkland, Advanced Computing in Electron Microscopy, 2010.

[28] K. Kuramochi, T. Yamazaki, Y. Kotaka, M. Ohtsuka, I. Hashimoto, K. Watanabe, Effect of chromatic aberration on atomic-resolved spherical aberration corrected STEM images, Ultramicroscopy. 110 (2009) 36–42. doi:10.1016/j.ultramic.2009.09.003.

[29] R.F. Loane, P. Xu, J. Silcox, Thermal vibrations in convergent-beam electron diffraction, Acta Crystallogr. Sect. A. 47 (1991) 267–278. doi:10.1107/S0108767391000375.

[30] P.N. Keating, Effect of invariance requirements on the elastic strain energy of crystals with application to the diamond structure, Phys. Rev. 145 (1966) 637–645. doi:10.1103/PhysRev.145.637.

[31] T.-C. Chiang, R. Ludecke, D.E. Eastman, Photoemission studies of AlGaAs(100) surfaces grown by molecular-beam epitaxy, Phys. Rev. B. 25 (1982) 6518–6521. doi:10.1103/PhysRevB.25.6518.

[32] A. Stall, J. Zilko, V. Swaminathan, N. Schumaker, Morphology of GaAs and AlGaAs grown by molecular beam epitaxy, J. Vac. Sci. Technol. B. 3 (1985).

[33] J.M. Moison, C. Guille, F. Houzay, F. Barthe, M. Van Rompay, Surface segregation of third-column atoms in group III-V arsenide compounds: Ternary alloys and heterostructures, Phys. Rev. B. 40 (1989) 6149–6162. doi:10.1103/PhysRevB.40.6149.

[34] O. Dehaese, X. Wallart, F. Mollot, Kinetic model of element III segregation during molecular beam epitaxy of III-III'-V semiconductor compounds, Appl. Phys. Lett. 66 (1995) 52–54. doi:10.1063/1.114180.

[35] J.M. Gerard, In situ probing at the growth temperature of the surface composition of (InGa)As and (InAl)As, Appl. Phys. Lett. 61 (1992) 2096–2098. doi:10.1063/1.108318.

[36] A. Rosenauer, D. Gerthsen, D. Van Dyck, M. Arzberger, G. Böhm, G. Abstreiter, Quantification of segregation and mass transport in InGaAs/GaAs Stranski-Krastanow layers, Phys. Rev. B. 64 (2001) 245334. doi:10.1103/PhysRevB.64.245334.

[37] M. Schowalter, A. Rosenauer, D. Gerthsen, M. Grau, M.C. Amann, Quantitative measurement of the influence of growth interruptions on the Sb distribution of GaSb/GaAs quantum wells by transmission electron microscopy, Appl. Phys. Lett. 83 (2003) 3123–3125. doi:10.1063/1.1618380.

[38] X. Li, Y. Zhang, D. Jiang, F. Guo, D. Wang, L. Zhao, Atomic intermixing and segregation at the interface of InAs/GaSb type II superlattices, Superlattices Microstruct. 104 (2017) 390–396. doi:10.1016/j.spmi.2017.02.052.

[39] T. Walther, C.J. Humphreys, D.J. Robbins, Diffusion and Surface Segregation in Thin SiGe/Si Layers Studied by Scanning Transmission Electron Microscopy, Defect Diffus.

Forum. 143–147 (1997) 1135–1140. doi:10.4028/www.scientific.net/DDF.143-147.1135.

[40] D.J. Norris, Y. Qiu, A. Dobbie, M. Myronov, T. Walther, Similarity of Stranski-Krastanow growth of Ge/Si and SiGe/Si (001), J. Appl. Phys. 115 (2014). doi:10.1063/1.4837975.

[41] R. Magri, A. Zunger, Effects of interfacial atomic segregation and intermixing on the electronic properties of InAs/GaSb superlattices, Phys. Rev. B - Condens. Matter Mater. Phys. 65 (2002) 1653021–16530218. doi:10.1103/PhysRevB.65.165302.

[42] S.D. Findlay, J.M. LeBeau, Detector non-uniformity in scanning transmission electron microscopy, Ultramicroscopy. 124 (2013) 52–60. doi:10.1016/j.ultramic.2012.09.001.

[43] K.A. Mkhoyan, S.E. Maccagnano-Zacher, E.J. Kirkland, J. Silcox, Effects of amorphous layers on ADF-STEM imaging, Ultramicroscopy. 108 (2008) 791–803. doi:10.1016/j.ultramic.2008.01.007.

[44] V. Grillo, The effect of surface strain relaxation on HAADF imaging, Ultramicroscopy. 109 (2009) 1453–1464. doi:10.1016/j.ultramic.2009.07.010.

[45] A. Beyer, L. Duschek, J. Belz, K. Jandieri, K. Volz, Influence of surface relaxation of strained layers on atomic resolution ADF imaging, Ultramicroscopy. 181 (2017) 8–16. doi:10.1016/j.ultramic.2017.04.019.

[46] A. Beyer, L. Duschek, J. Belz, J.O. Oelerich, K. Jandieri, K. Volz, Surface relaxation of strained Ga(P,As)/GaP heterostructures investigated by HAADF STEM, J. Microsc. 268 (2017) 239–247. doi:10.1111/jmi.12622.

[47] L. Duschek, P. Kükelhan, A. Beyer, S. Firoozabadi, J.O. Oelerich, A. Ballabio, G. Isella, K. Volz, Composition determination of semiconductor alloys towards atomic accuracy by HAADF-STEM, Submitt. to Ultramicroscopy. (2018).

[48] K. Levenberg, A Method for the Solution of Certain Non-Linear Problems in Least Squares, Q. Appl. Math. 2 (1944) 164–168. doi:10.1090/qam/10666.

[49] J.A. Nelder, R. Meadf, A simplex method for function minimization, Comput. J. 7 (1964) 308–313.

[50] J. Belz, A. Beyer, T. Torunski, W. Stolz, K. Volz, Direct investigation of (sub-) surface preparation artifacts in GaAs based materials by FIB sectioning, Ultramicroscopy. 163 (2016) 19–30. doi:10.1016/j.ultramic.2016.01.001.

[51] T. Grieb, M. Tewes, M. Schowalter, K. Müller-Caspary, F.F. Krause, T. Mehrtens, J.M. Hartmann, A. Rosenauer, Quantitative HAADF STEM of SiGe in presence of amorphous surface layers from FIB preparation, Ultramicroscopy. 184 (2018) 29–36. doi:10.1016/j.ultramic.2017.09.012.

[52] R.R. Cerchiara, P.E. Fischione, J. Liu, J.M. Matesa, A.C. Robins, H.L. Fraser, A. Genc, Raising the Standard of Specimen Preparation for Aberration-Corrected TEM and

STEM, Micros. Today. 19 (2011) 16–19. doi:10.1017/S1551929510001197.

[53] R.F. Egerton, Electron Energy-Loss Spectroscopy in the Electron Microscope, 3rd ed., 2011.

[54] Y. Mizokawa, O. Komoda, S. Miyase, Long-time air oxidation and oxide-substrate reactions on GaSb, GaAs, adn GaP at room temperature studied by x-ray photoelectron spectroscopy, Thin Solid Films. 156 (1988) 127–143. doi:10.1016/0040-6090(88)90288-X.

Figure captions

Table 1: Parameters used for simulation of *(GaIn)As* and *Ga(AsSb)* with varying composition. The parameters were determined from the electron microscope used.

Fig. 1: HAADF-STEM images of the single *(GaIn)As-QW* (A) and the single *Ga(AsSb)*-QW (C). The intensity in both images is normalized to the impinging beam. Magnified insets show the high resolution. Composition maps of the single *(GaIn)As*-QW and the single *Ga(AsSb)*-QW are shown in (B) and (D), respectively. The number of *In* respectively *Sb* is given per atomic column with atomic resolution. Note, that the total number of atoms per column (i.e. the thickness) is not constant within the image. Negative compositions are explained in the main text. Growth direction is from left to right.

Fig. 2: HAADF-STEM image of the "W"-QWH (A). The intensity is normalized to the impinging beam. A magnified inset shows the high resolution. The composition of *In* is shown in B, while the composition of *Sb* is presented in C. Again, note the varying thickness of the atomic columns. Negative compositions are explained in the text. Growth direction is from left to right.

Fig. 3: Muraki model fitted to the composition profiles of the single *(GaIn)As*-QW (A), the first *(GaIn)As*-QW in the "W"-QWH (B) and the second *(GaIn)As*-QW in the "W"-QWH. The concentration of *In* is given as fraction averaged over one atomic layer considering the local thickness of each atomic column. Shown error bars do not indicate the error of composition determination but the standard deviation per lattice plane. Fit parameters are given as insets.

Fig. 4: Muraki model fitted to the composition profiles of the single *Ga(AsSb)*-QW (A) and the *Ga(AsSb)*-QW in the "W"-QWH (B). The concentration of *Sb* is given as fraction averaged over one atomic layer considering the local thickness of each atomic column. Shown error bars do not indicate the error of composition determination but the standard deviation per lattice plane. Fit parameters are given as insets.

Fig. 5: F3LE model fitted to *(GaIn)As*-QWs. The results for the single QW (A) and the first (B) and second (C) QW in the "W"-QWH are shown together with the parameters used. Energies are given in eV. The parameter N describes the layer after which *In* deposition stops.

Fig. 6: F3LE model fitted to single *Ga(AsSb)*-QW (A) and *Ga(AsSb)*-QW in the "W"-QWH (B). The fitting parameters are given as insets. Energies are given in eV. The parameter N describes the layer after which *Sb* deposition stops.

Fig. 7: Modified Muraki model with two different segregation coefficients fitted to the concentration profiles of the first (A) and the second (B) *(GaIn)As*-QW in the "W"-QWH. In both cases, a reasonable description of both interfaces is reached. Fit parameters are given as insets.

Table(s)

Electron energy	200 kV
Aperture angle	21.3 mrad
Two-fold astigmatism	0 nm
C_S	2 µm
C_5	5 mm
C_C	1.5 mm

Figure(s)

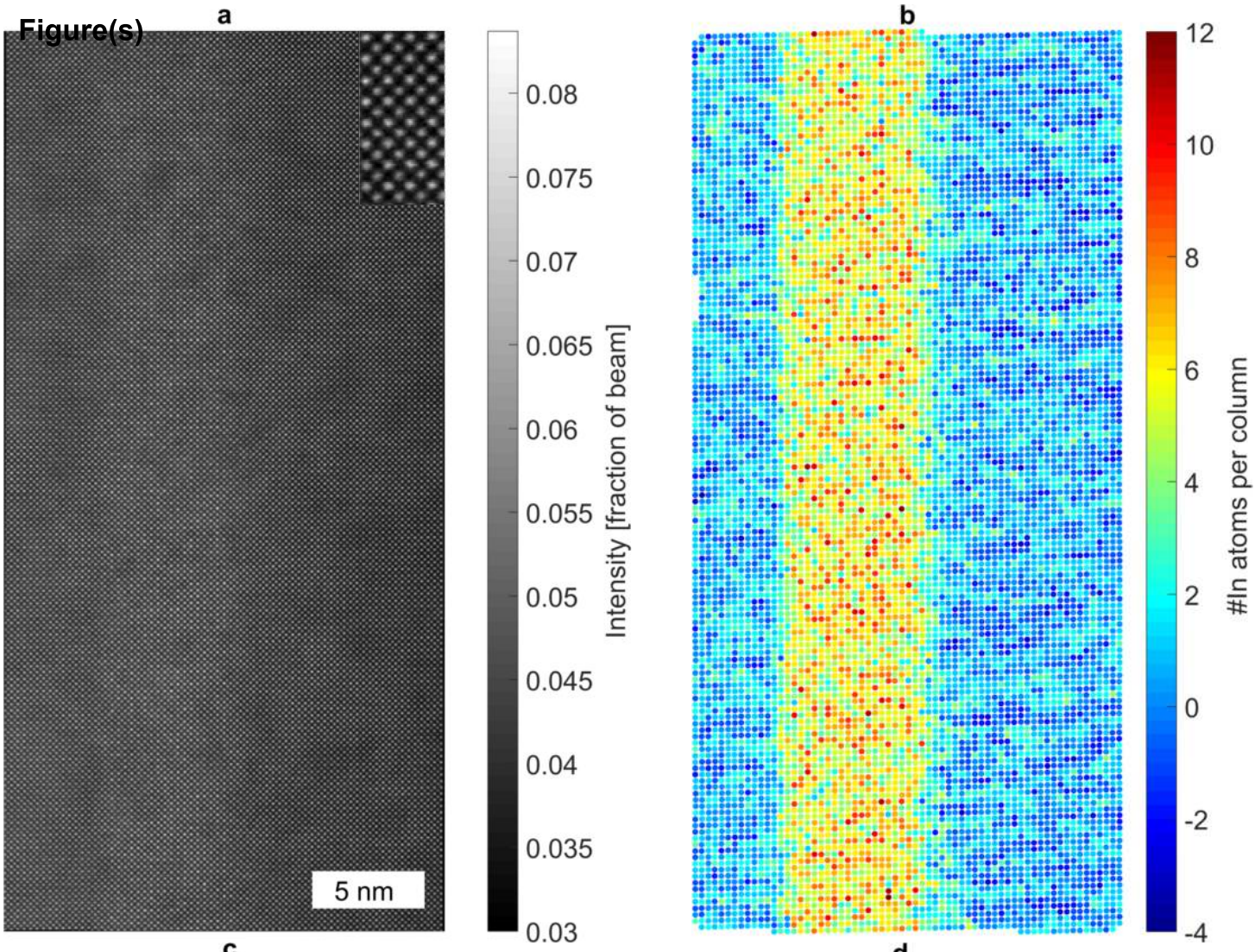
a
5 nm
0.08
0.075
0.07
0.065
0.06
0.055
0.05
0.045
0.04
0.035
0.03
Intensity [fraction of beam]
b
12
10
8
6
4
2
0
-2
-4
#In atoms per column

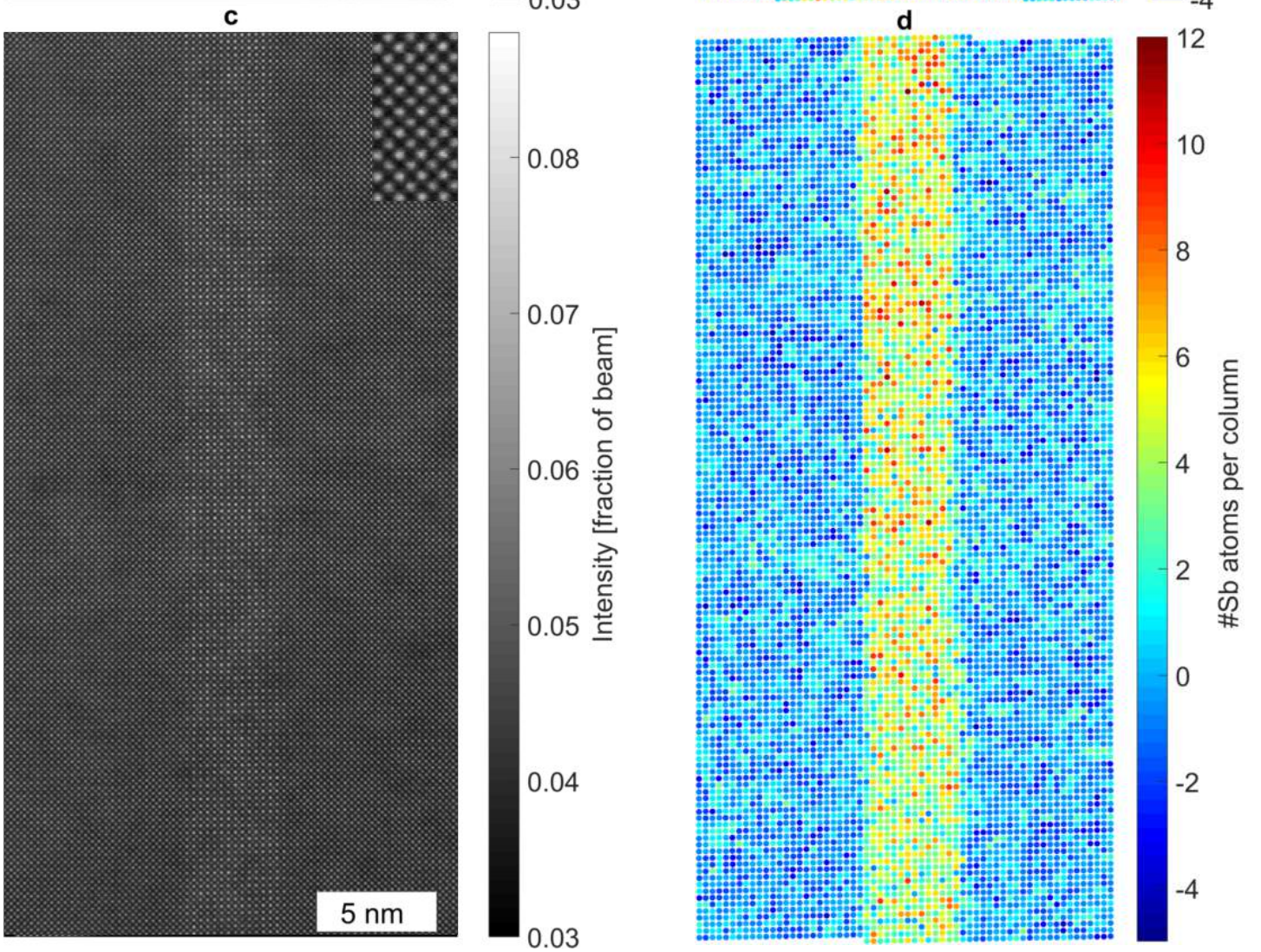
c
5 nm
0.08
0.07
0.06
0.05
0.04
0.03
Intensity [fraction of beam]
d
12
10
8
6
4
2
0
-2
-4
#Sb atoms per column

Figure(s)

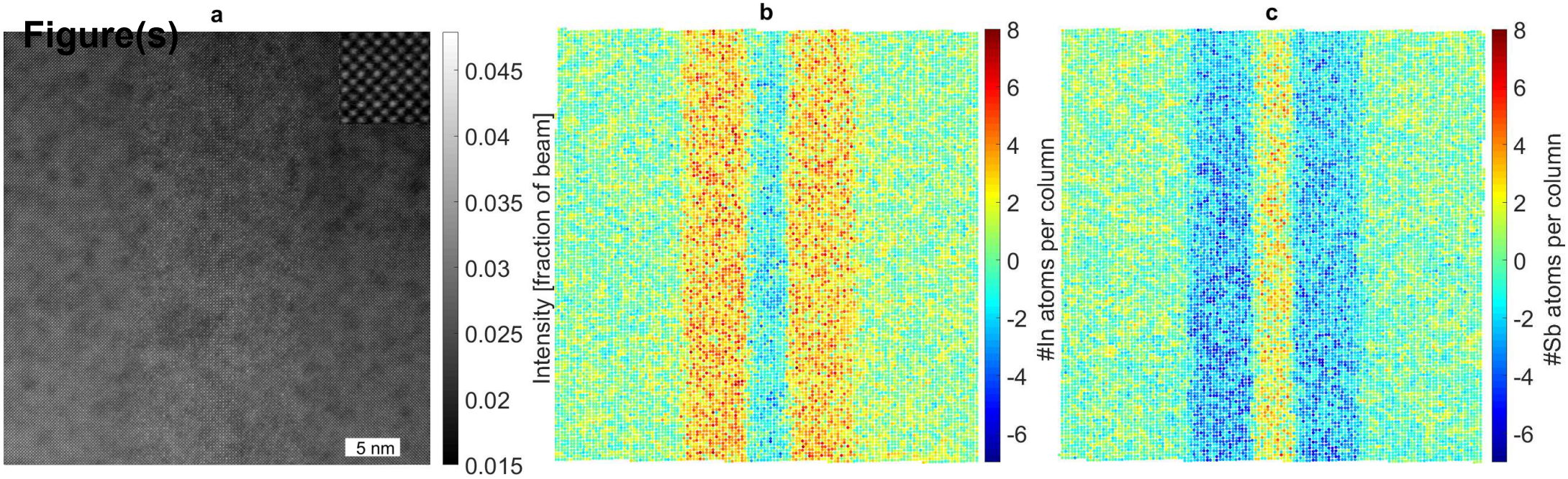
a
5 nm
0.045
0.04
0.035
0.03
0.025
0.02
0.015
Intensity [fraction of beam]
b
8
6
4
2
0
-2
-4
-6
#In atoms per column
c
8
6
4
2
0
-2
-4
-6
#Sb atoms per column

Figure(s)

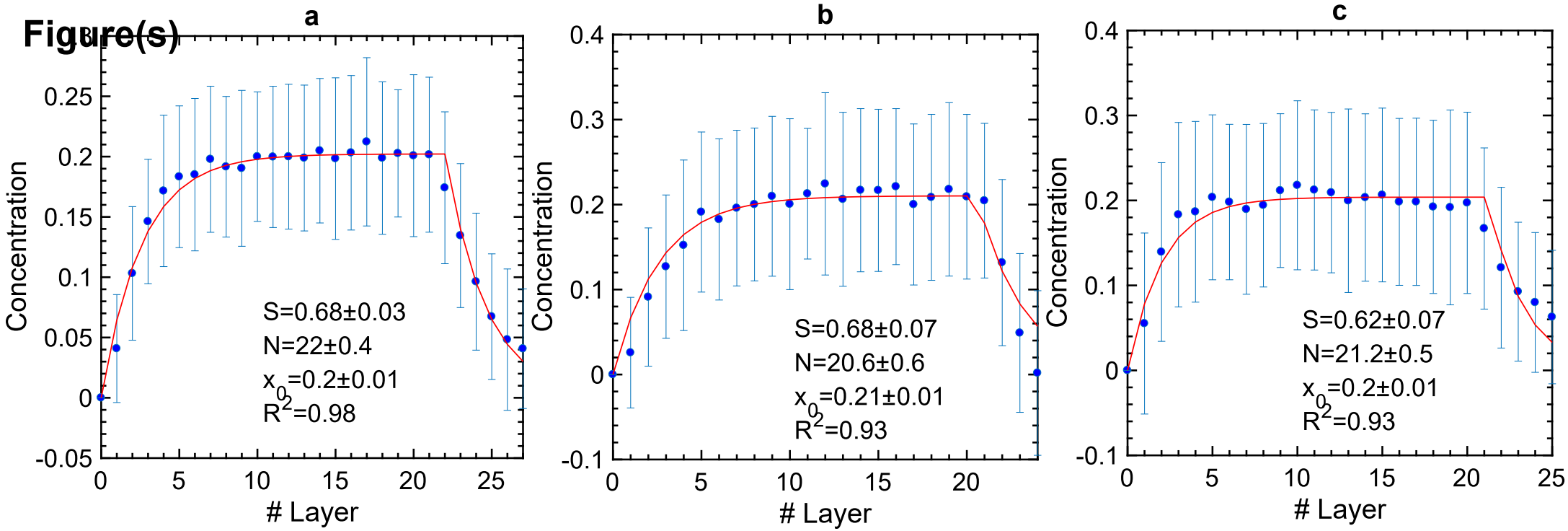
a
b
c
Concentration
# Layer
S=0.68±0.03
N=22±0.4
x0=0.2±0.01
R2=0.98
S=0.68±0.07
N=20.6±0.6
x0=0.21±0.01
R2=0.93
S=0.62±0.07
N=21.2±0.5
x0=0.2±0.01
R2=0.93

Figure(s)

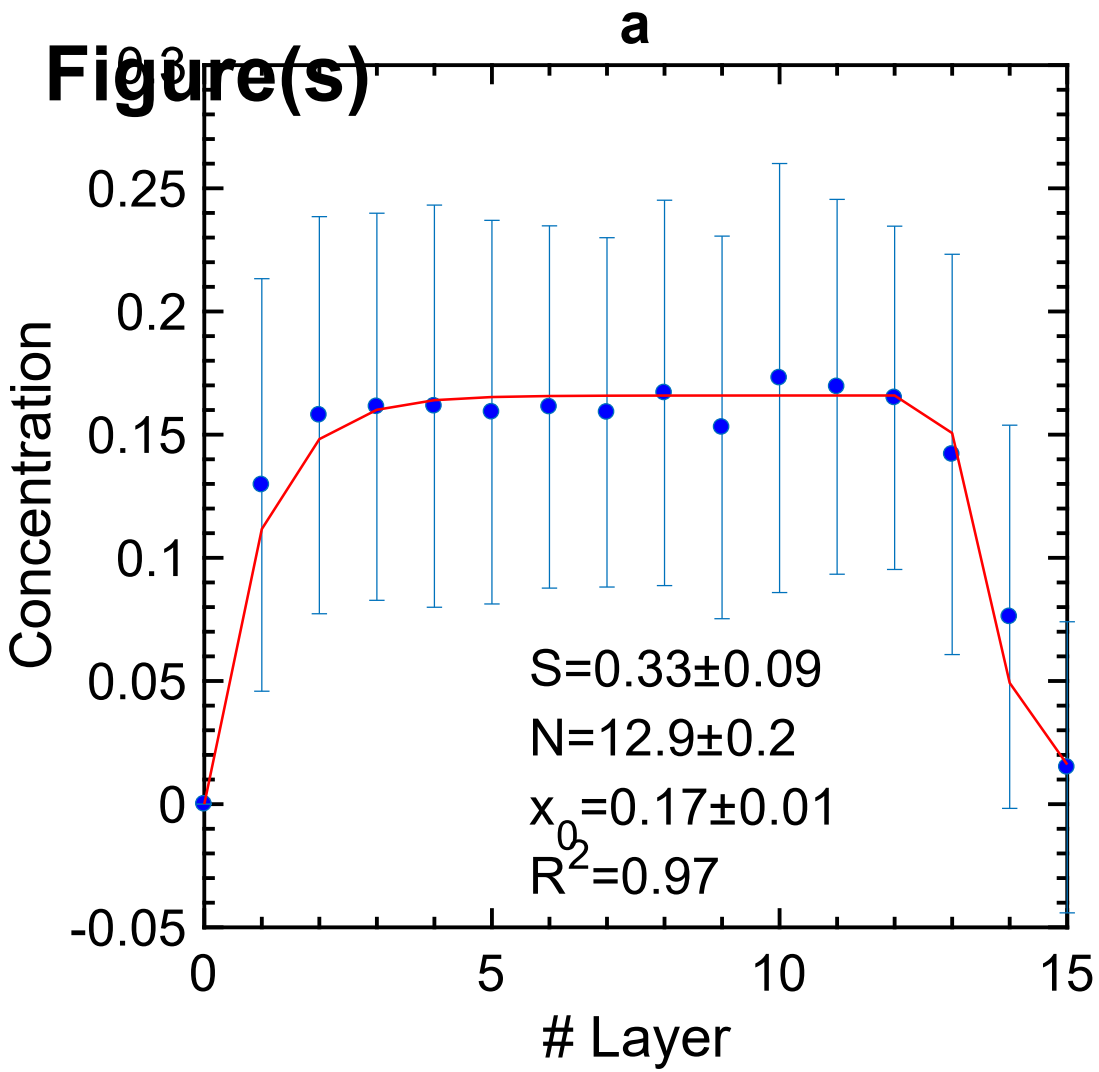
a
Concentration
# Layer
S=0.33±0.09
N=12.9±0.2
x0=0.17±0.01
R2=0.97

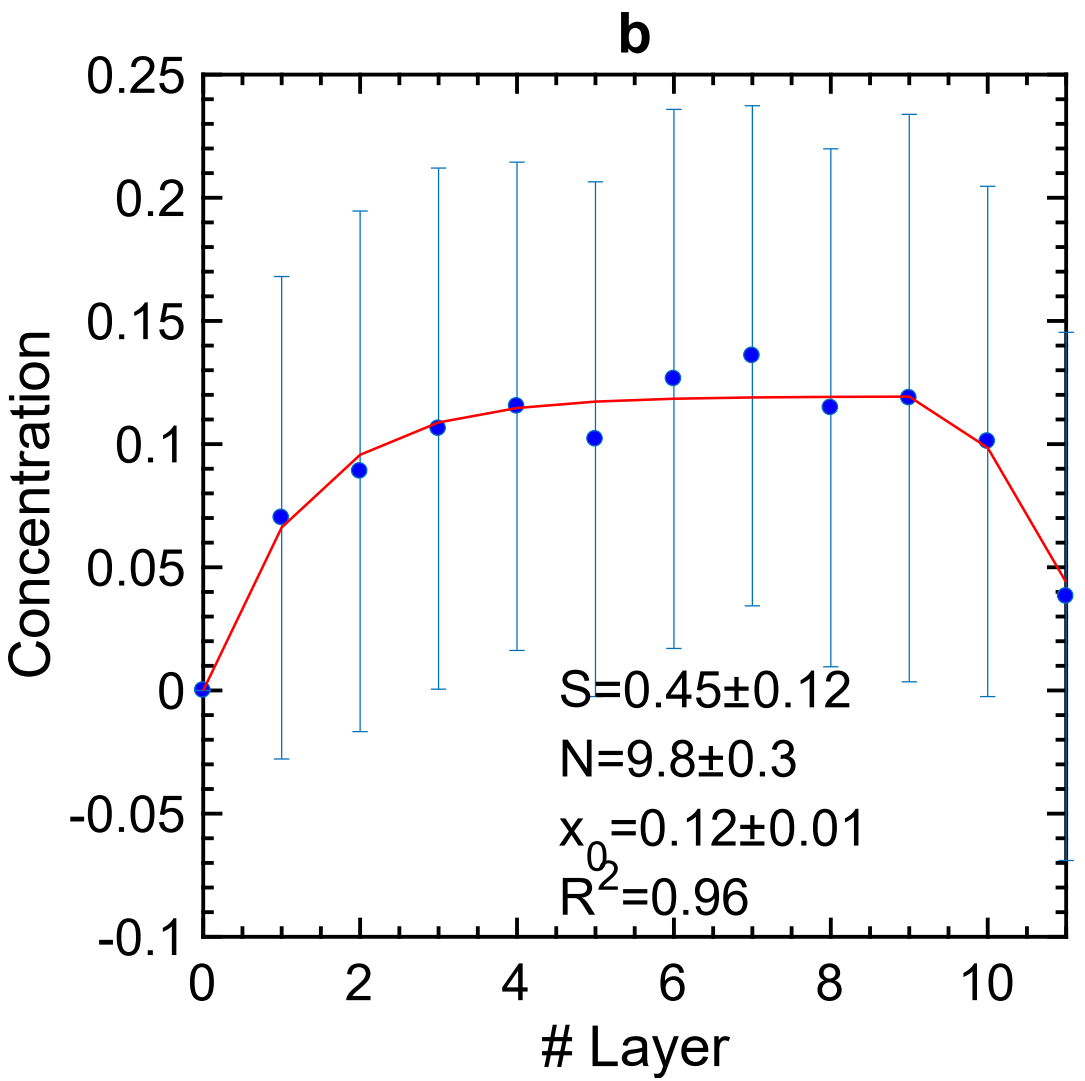
b
Concentration
# Layer
S=0.45±0.12
N=9.8±0.3
x0=0.12±0.01
R2=0.96

Figure(s)

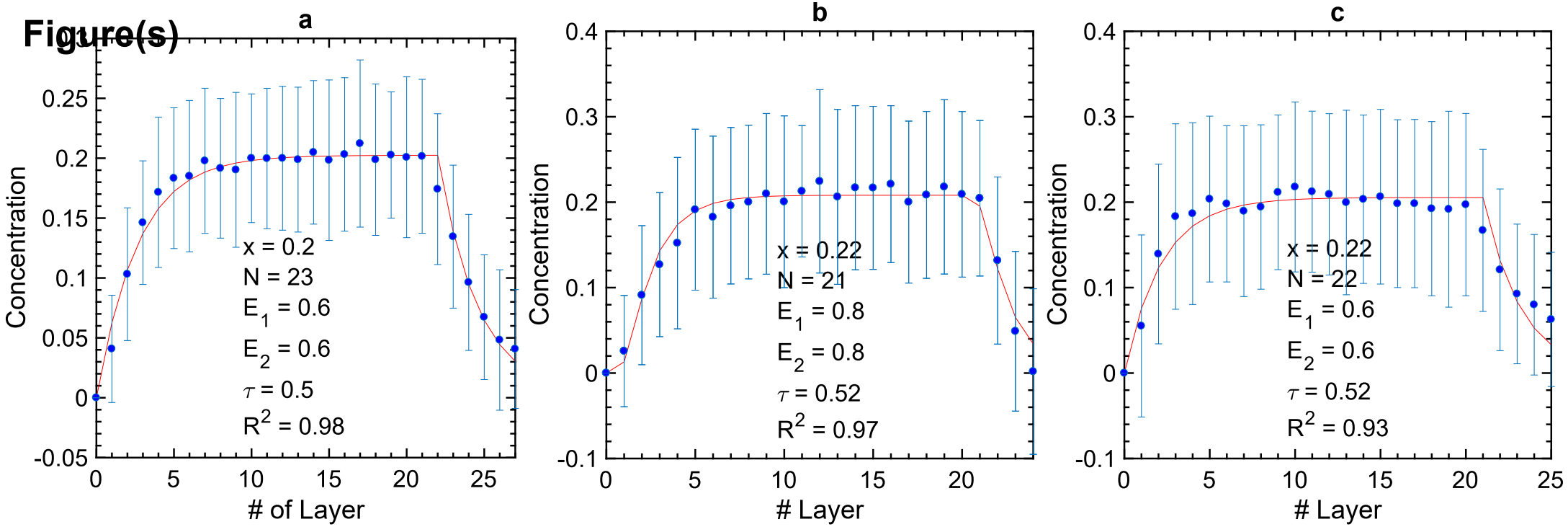
a
b
c
Concentration
# of Layer
# Layer
x = 0.2
N = 23
E1 = 0.6
E2 = 0.6
τ = 0.5
R2 = 0.98
x = 0.22
N = 21
E1 = 0.8
E2 = 0.8
τ = 0.52
R2 = 0.97
x = 0.22
N = 22
E1 = 0.6
E2 = 0.6
τ = 0.52
R2 = 0.93

Figure(s)

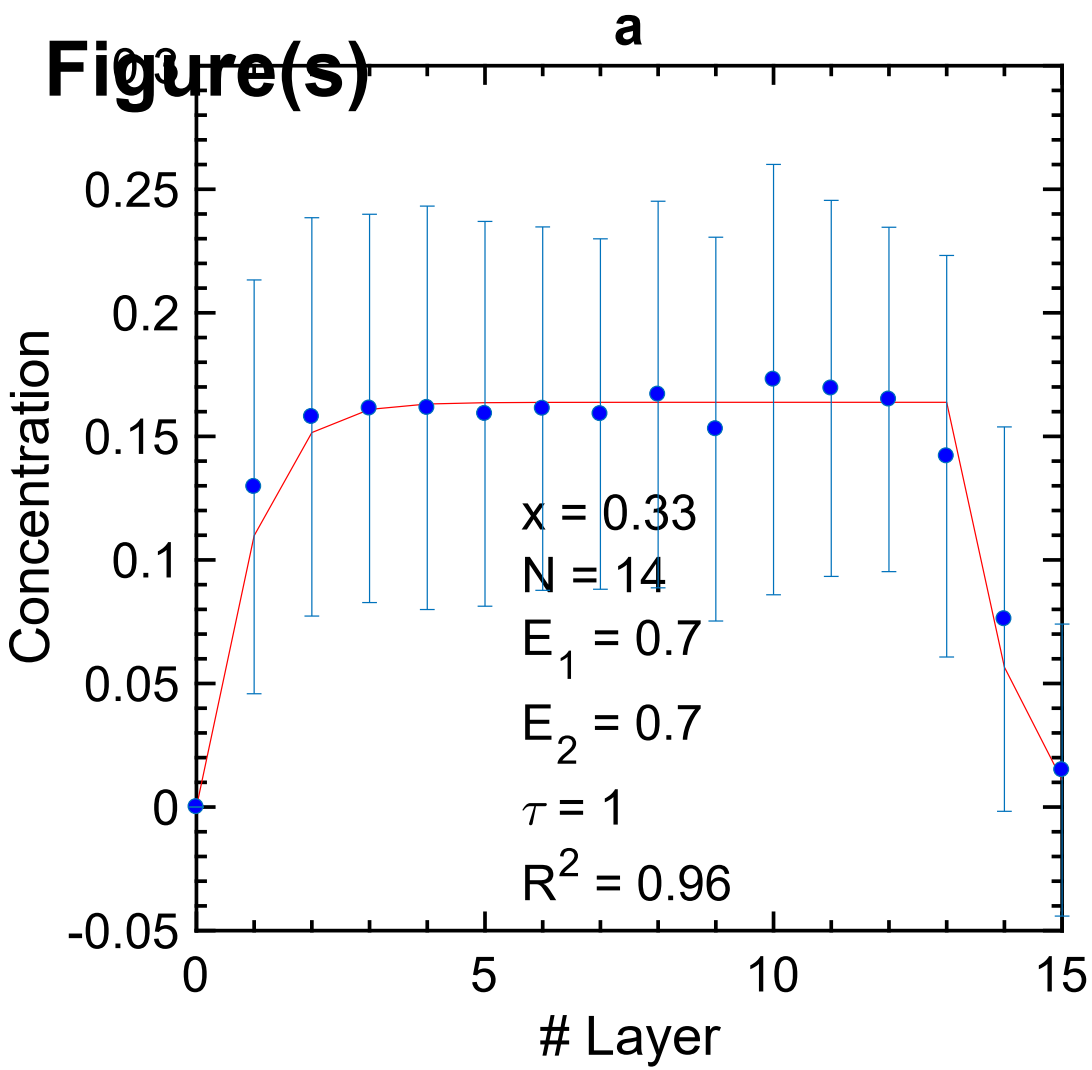
a
Concentration
# Layer
x = 0.33
N = 14
E1 = 0.7
E2 = 0.7
τ = 1
R2 = 0.96

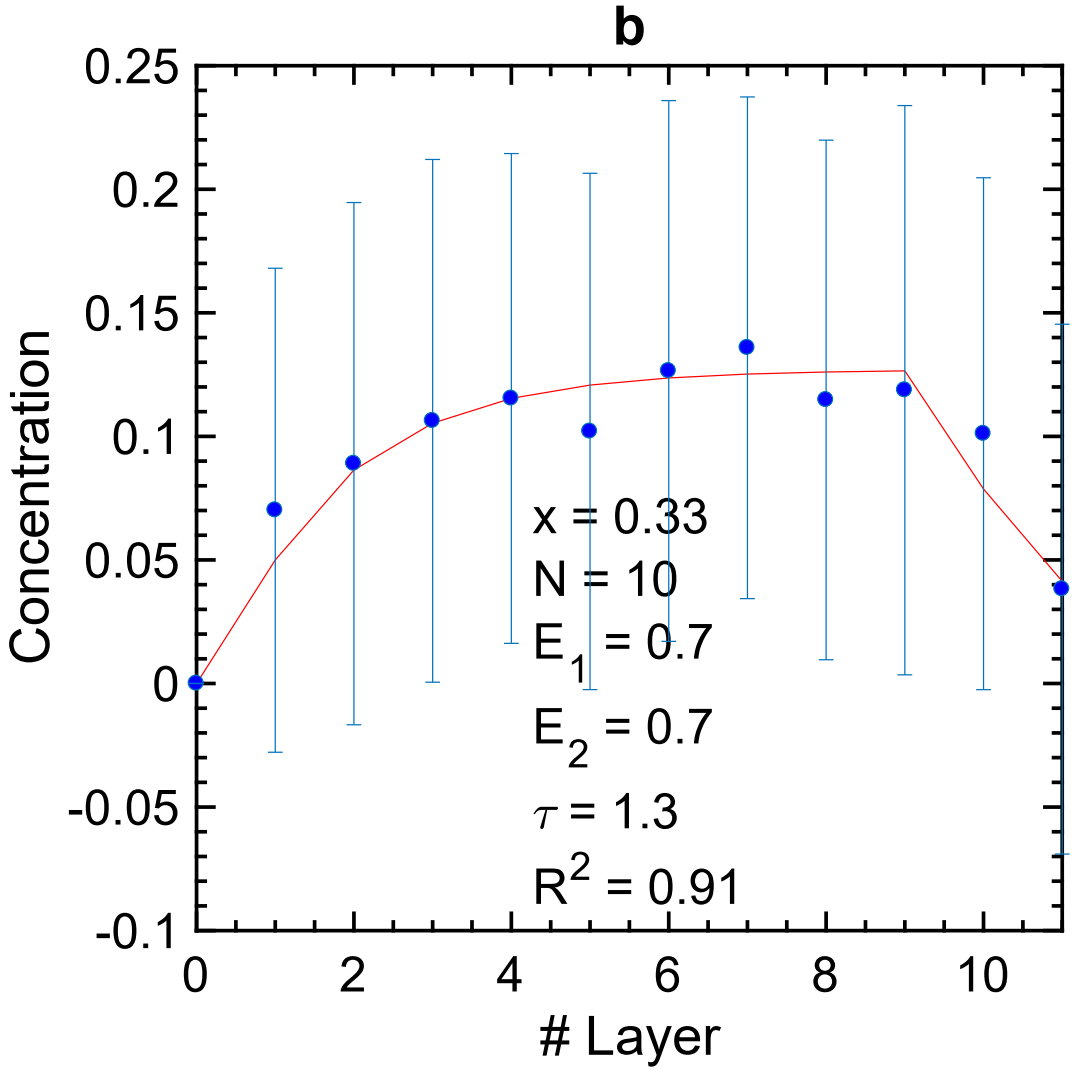
b
Concentration
# Layer
x = 0.33
N = 10
E1 = 0.7
E2 = 0.7
τ = 1.3
R2 = 0.91

Figure(s)

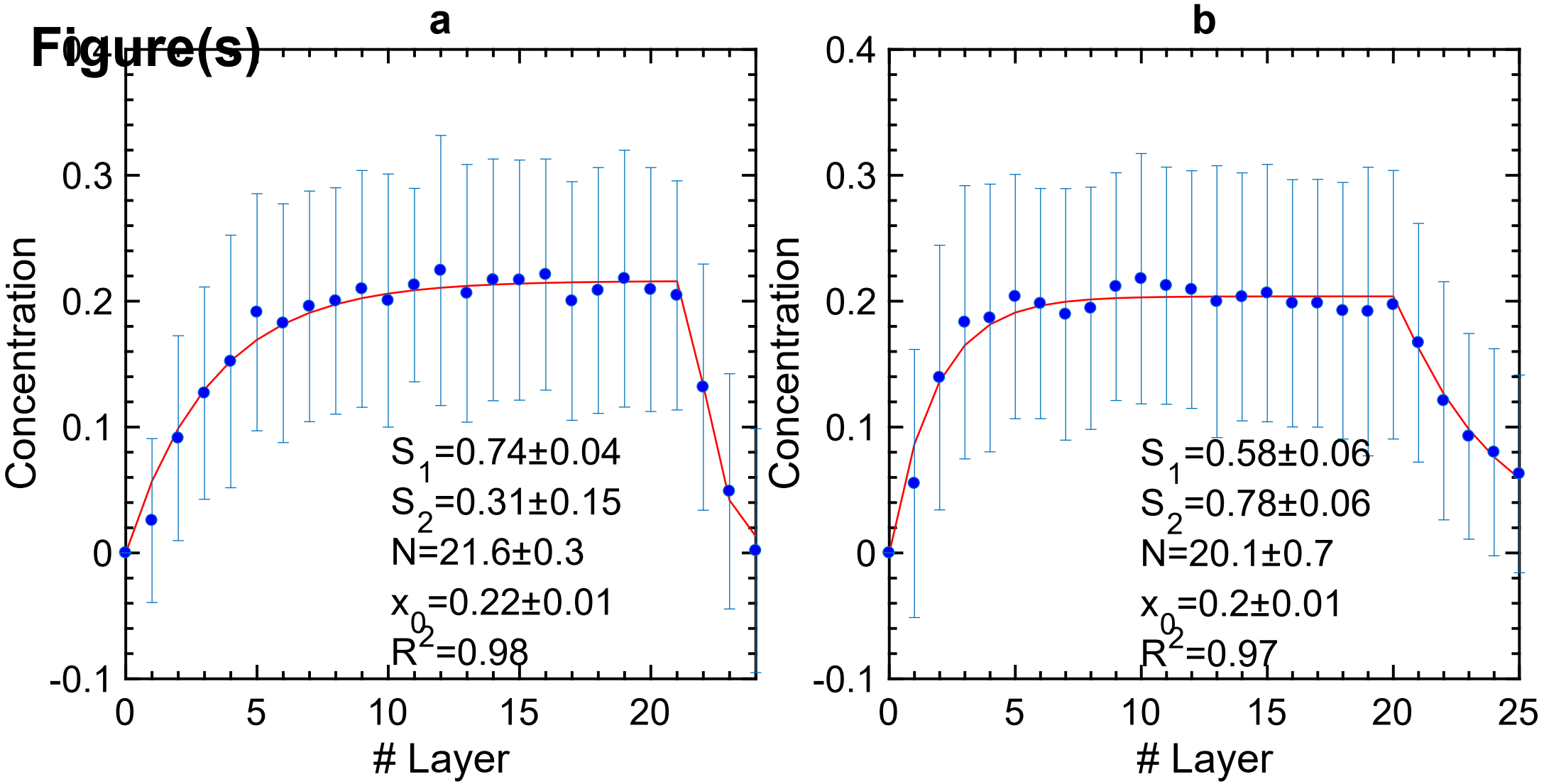
a
b
Concentration
# Layer
S1=0.74±0.04
S2=0.31±0.15
N=21.6±0.3
x0=0.22±0.01
R2=0.98
S1=0.58±0.06
S2=0.78±0.06
N=20.1±0.7
x0=0.2±0.01
R2=0.97